Design and Performance Analysis of a Torque-Based Optical Fiber Flow Sensor

Hao Hu[*], Liqiong Zhong

College of Mechanical Engineering, Guiyang University, 550003 Guiyang, China

[*] Correspondence: Hao Hu (haohu0105@126.com)

Abstract: A torque-based optical fiber flow sensor has been designed and experimentally tested to assess its potential for fluid flow measurement. The sensor utilizes an optical fiber strength modulation principle to achieve flow detection. Detailed attention is given to the design of the sensor structure, including the sensor probe and fiber bundle probe, and the working principle of the torque-based flow sensor is systematically described. A theoretical model of the sensor is established, considering key parameters such as torque (m), radius (r), sensor joint stiffness (S_J), refractive index (n), and radius of curvature (R), which significantly affect its detection performance. Simulations are conducted to obtain Q-M curves under varying parameter conditions, revealing the relationship between sensor output and fluid flow rate. A gas flow detection experiment is subsequently performed on a custom-built experimental platform to evaluate the sensor's practical performance. The results indicate that the sensor output decreases monotonically with increasing fluid flow for different parameter settings, demonstrating a good linear response within a specific detection range. It is found that the sensitivity of the sensor is influenced by the selection of critical performance parameters and the characteristics of the fluid being measured. For gas flow detection, the sensor output voltage shows an approximately linear decrease with the increase in gas flow. The comparison between simulation and experimental data confirms that both exhibit similar trends, thereby validating the sensor's applicability in fluid flow detection. This study highlights the potential of torque-based optical fiber flow sensors for accurate and reliable fluid flow measurements.

Keywords: Torque-based; Optical fiber; Flow sensor; Design; Experiment; Fluid flow detection; Sensitivity analysis; Simulation

1 Introduction

Flow sensors are widely used across various fields, including industrial production, energy measurement, environmental monitoring, pipeline transportation, biotechnology, scientific experiments, and marine meteorology, making them a critical component among sensor technologies. Due to their significance, research on flow sensors has attracted substantial attention [1–4]. In parallel, optical fiber sensing technology has experienced rapid advancements in recent years due to its numerous advantages, such as high sensitivity, resistance to electromagnetic interference, and flexibility in harsh environments [5–19]. Consequently, there has been growing interest in applying fiber optic sensing technology to flow sensors [19–22]. However, research in this area remains limited, the associated technologies are not yet fully developed, and further in-depth and innovative studies are necessary to advance this field. In response to these challenges, a torque-based optical fiber flow sensor structure is proposed in this study. This sensor design utilizes the deflection of a torque body under fluid flow, coupled with a matrix-arranged fiber beam probe, to convert fluid flow detection into the measurement of light intensity received by the fiber. This approach introduces a novel method for applying fiber optic sensing technology to fluid flow detection and provides valuable insights for further research and development of optical fiber flow sensors.

2 Sensor Design

2.1 Sensor Probe Design

The structure of the probe in the torque-based optical fiber flow sensor is illustrated in Figure 1. The sensor probe is housed in a mechanical assembly comprising an external shell, a torque body, a corrugated sealing bag, bearings, and rollers. The sensor's outer shell consists of symmetrical left and right sections. The torque body, which is driven

by fluid forces, is integrated into the shaft assembly hole via bearings. Separate assembly holes are provided for securing the incident and receiving fiber probes, ensuring the proper alignment and reconnection of the incident fiber probe, the receiving fiber probe, and the light transmission hole during the assembly process. The lower roller of the torque body operates within a circular roller guide groove, which functions to support and position the torque body accurately. At the bottom end of the torque body, the force plate is positioned centrally within the fluid detection channel, enabling the detection of moments exerted by the flowing fluid. Figure 2 depicts the structural diagram of the torque body, which includes components such as the upper rotating shaft, the upper neck, the light shield, the light transmission hole, the lower neck, the lower rolling shaft, and the force plate. The light transmission hole, located in the middle and upper sections of the light shield, is designed to match the geometric size and shape of the end face of the optical fiber bundle. The force plate, circular in shape, experiences normal thrust under fluid action, causing the torque body to deflect at a specific angle. The torque body reaches a new equilibrium position when the fluid pressure balances the normal component of the torque force.
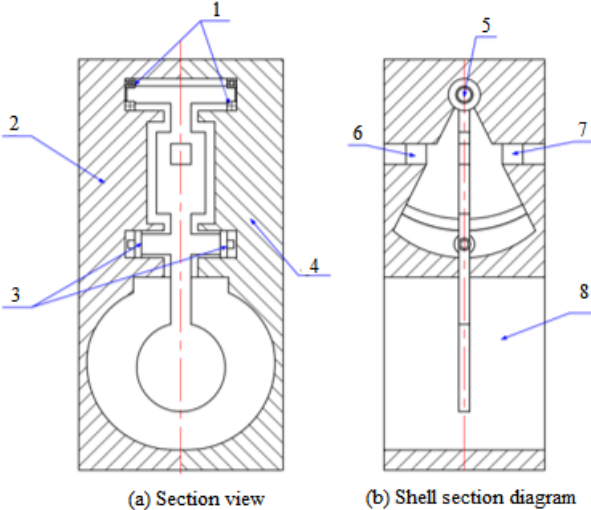

Figure 1. Sensor probe

Note: 1. Bearing; 2. Left shell; 3. Roller; 4. Right shell; 5. Shaft assembly hole; 6 and 7. Assembly holes for the incident optical fiber and the receiving optical fiber; 8. Check the fluid channel
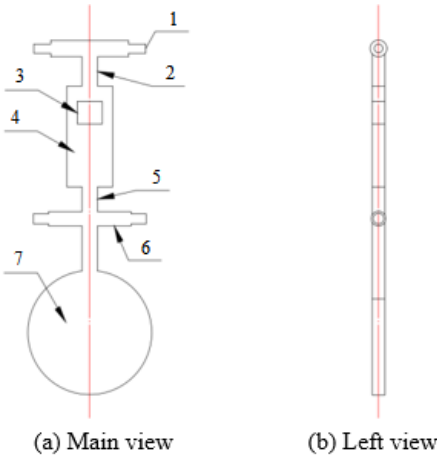

Figure 2. Torque body structure

Note: 1. Upper rotation shaft; 2. Upper neck; 3. Light transmission hole; 4. Shading plate 5. Lower neck; 6. Lower roll shaft; 7. Bearing plate

2.2 Design of Optical Fiber Probe

As illustrated in Figure 3, the cross-sections of both the incident fiber probe and the receiving fiber probe in the sensor feature a rectangular array structure, comprising tightly arranged incident and receiving fiber bundles. These bundles consist of multiple multimode fibers with small core diameters. The geometric shape and size of the two fiber

bundles are identical, and the geometric parameters of the light transmission hole on the mask are also consistent with these dimensions.
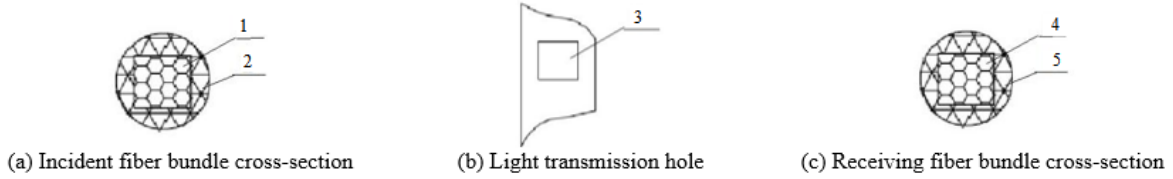

(a) Incident fiber bundle cross-section   (b) Light transmission hole   (c) Receiving fiber bundle cross-section

Figure 3. Cross section of optical fiber bundle

Note: 1, 4. Rectangular optical fiber bundle array; 2, 5. Optical fiber bundle cladding; 3. Light transmission holes

2.3 Working Principle of the Sensor

Figure 4 presents a schematic diagram illustrating the change in the effective receiving end face of the receiving fiber bundle during sensor detection. In subgraph (a) of Figure 4, at the initial position, the light emitted from the incident fiber bundle passes through the light transmission hole, fully illuminating the entire receiving end face of the receiving fiber bundle. In subgraph (b) of Figure 4, when fluid flow is detected, the torque body generates torque due to the fluid's action, causing the light mask to partially block the receiving end face of the receiving fiber bundle. This blockage alters the effective area of light intensity reception, resulting in a change in the output light intensity. By measuring this change in light intensity, the angle of the torque body can be calculated, and subsequently, the fluid pressure on the force plate is determined. Based on the quantitative relationship between pressure and flow, the flow rate of the measured fluid can then be accurately calculated.
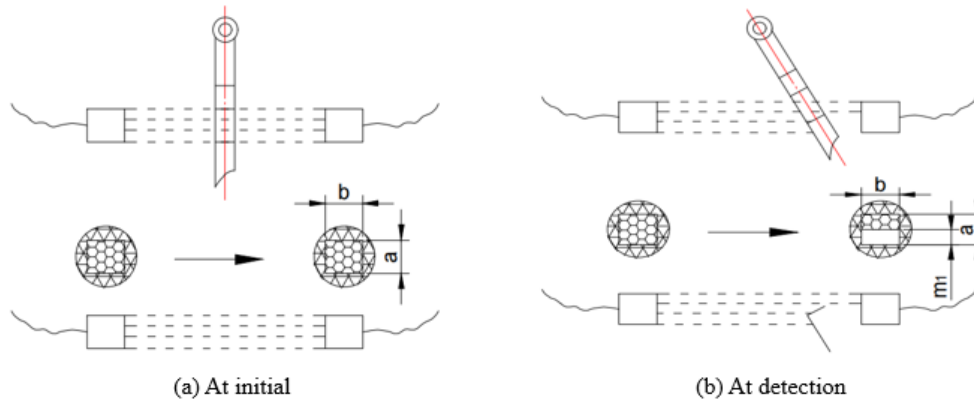

(a) At initial   (b) At detection

Figure 4. Schematic diagram of fiber bundle detection

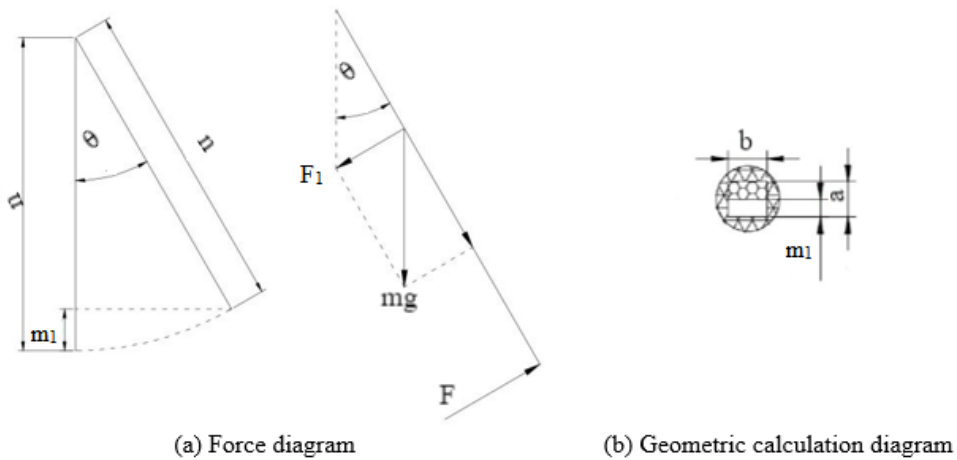(a) Force diagram   (b) Geometric calculation diagram

Figure 5. Sensor modeling analysis diagram

3 Mathematical Modeling

As shown in Figure 5, each analysis diagram required for sensor modeling calculation is shown. Subgraph (a) of Figure 5 is torque body force diagram and subgraph (b) of Figure 5 is geometric calculation diagram of occluding area.

Assuming that the pressure exerted by the fluid on the torque body is P, the flow rate of the fluid is v, the density of the fluid is ρ, the force area of the stress plate is S_B, and the radius of the stress plate is r, the following relationships can be derived based on fluid mechanics:

$$P = k\frac{\rho}{2}v^2 S_B \tag{1}$$

where, k is the proportional coefficient, $S_B = \pi r^2$.

And because the fluid flow rate is:

$$Q = Av \tag{2}$$

In the formula, A is the annular gap flow area formed between the fluid detection channel and the gravity rod bearing plate. Assuming the radius of the channel is R, then there is $A = \pi\left(R^2 - r^2\right)$ then Eqs. (1) and (2) can be combined into:

$$Q = \left(R^2 - r^2\right)\sqrt{\frac{2\pi P}{k\rho r^2}} \tag{3}$$

As shown in subgraph (a) of Figure 5, let the mass of the gravity rod be m, and when the Angle of θ is rotated under the action of fluid pressure F, the component of its gravity in the normal direction is:

$$F_1 = mg\sin\theta \tag{4}$$

At this time, because the force is balanced, there are:

$$F = F_1 \tag{5}$$

And there is $P.\pi r^2 = mg\sin\theta$.

So the rotation Angle is:

$$\theta = \arcsin\left(\frac{P\pi r^2}{mg}\right) \tag{6}$$

As shown in subgraph (b) of Figure 5, the effective receiving area of the receiving end face of the receiving fiber bundle is:

$$S_{J1} = a\left(b - m_1\right) \tag{7}$$

where, S_{J1} is the effective receiving area of the receiving end face of the receiving optical fiber bundle, m_1 is the height at which the receiving end face of the receiving optical fiber bundle is blocked, b is the height of the receiving end face of the receiving optical fiber bundle, and a is the width of the receiving optical fiber bundle.

$$m_1 = n\left(1 - \cos\arcsin\left(\frac{P\pi r^2}{mg}\right)\right) \tag{8}$$

The fiber intensity modulation model of the sensor can be expressed as the ratio of the effective receiving end area of the receiving fiber bundle to the total end area:

$$M = \frac{S_{J1}}{S_J} = \frac{a\left(b - m_1\right)}{ab} = \frac{b - n\left(1 - \cos\arcsin\left(\frac{P\pi r^2}{mg}\right)\right)}{b} \tag{9}$$

where, S_J is the end area of the fiber bundle, and n is the distance from the center of the rotating shaft on the gravity swinging rod to the lower edge of the light transmission hole.

It can also be obtained from Eq. (3) that:

$$P = \frac{k\rho r^2}{2\pi} \cdot \left(\frac{Q}{R^2 - r^2} \right)^2 \tag{10}$$

By substituting Eq. (10) into Eq. (9), we have:

$$M = 1 - \frac{n}{b} \left(1 - \cos\arcsin\left(\frac{k\rho r^2 \cdot \left(\frac{Q}{R^2-r^2} \right)^2 \cdot \pi r^2}{mg} \right) \right) \tag{11}$$

The above Eq. (11) represents the sensing model of the sensor. It is evident from the formula that, once the sensor's package structure and geometric dimensions are fixed, the output value M is solely dependent on the flow rate Q of the measured fluid. This indicates that the sensor's output value effectively reflects changes in the flow rate of the measured fluid.

4 Simulation Results and Analysis

Based on the sensor model discussed above, an analysis was conducted to determine the primary parameters influencing the sensor's detection performance. These parameters include the mass mmm of the torque body, the radius r of the stress plate, the end face area S_J of the fiber bundle, the distance n from the rotation axis of the torque body to the lower edge of the light transmission hole, the radius R of the fluid detection channel, and the density ρ of the fluid, among others. Simulations were performed using software to generate $Q - M$ curves for different values of each parameter. These simulations reveal the influence trends of each parameter on the sensor's output, providing insights into how each parameter affects the sensor's characteristics.

During the experiment, $Q - M$ curves were generated for the parameters m, r, S_J, n, R and ρ by varying one parameter at a time while keeping the others constant. The resulting $Q - M$ curves for different parameter values are presented in Figure 6 to Figure 11, respectively.

From Figure 6 to Figure 11, it can be observed that the output values of the sensor decrease monotonically as the flow rate of the measured fluid increases, with the rate of decrease accelerating at higher flow rates. This behavior occurs because the initial output value of the sensor corresponds to the maximum received light intensity at the receiving fiber's end face, which, after normalization, is set to 1. During detection, as the light baffle rotates, a portion of the receiving fibers becomes blocked, reducing the received light intensity. Following normalization, the output value gradually decreases from 1. Additionally, the sensor demonstrates good linearity within a certain detection range.
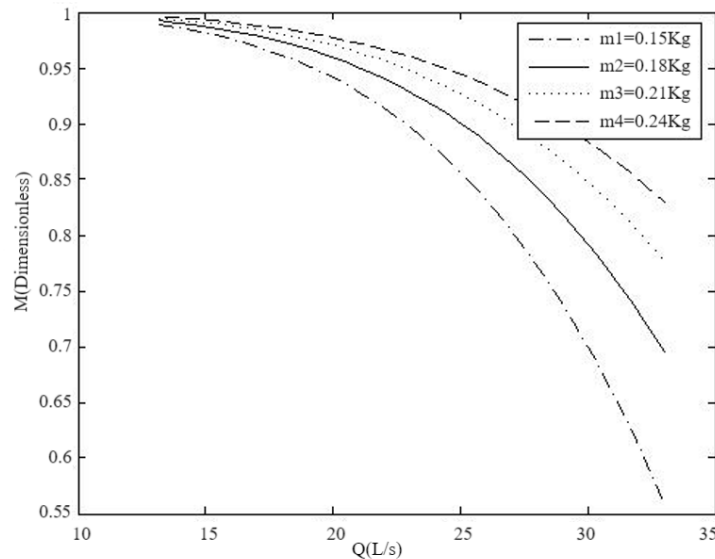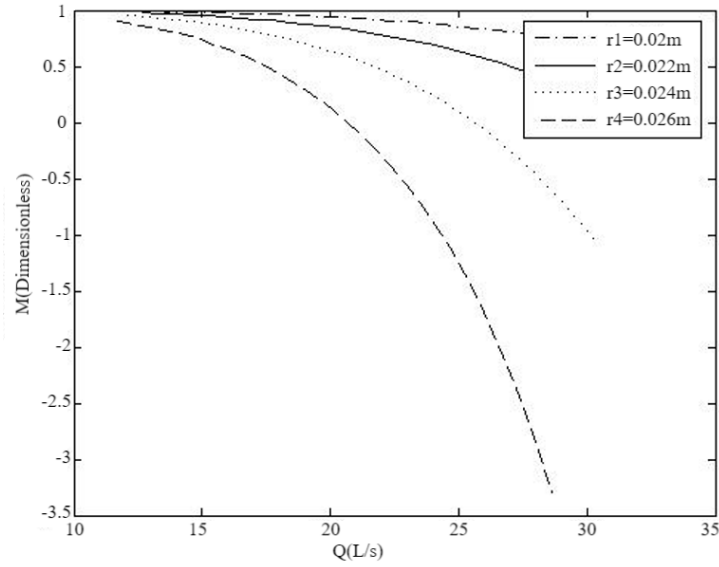

Figure 6. $Q - M$ Curve with change of m value

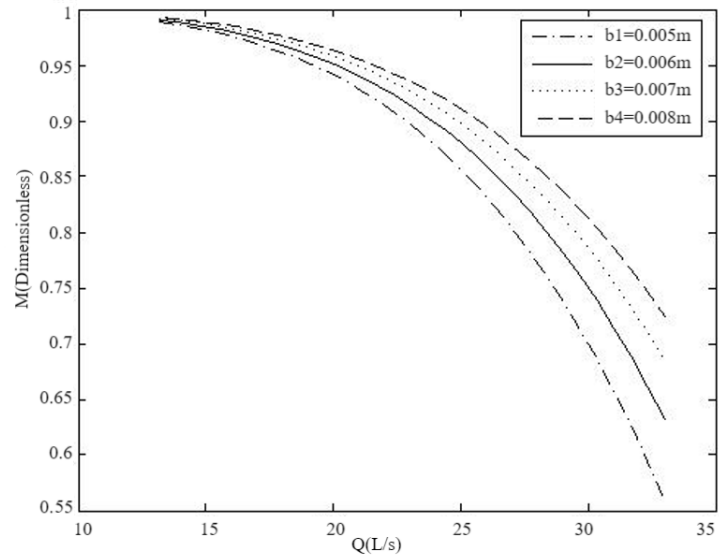**Figure 7.** $Q - M$ Curve with change of r value

Figure 8. $Q - M$ Curve with change of b value

As shown in Figure 6, the $Q - M$ characteristic curves of the sensor were generated for different torque body masses mmm of 0.15 kg, 0.18 kg, 0.21 kg, and 0.24 kg. The remaining parameters used in the calculations were set to r=0.02 m, $S_J = 5 \times 10^{-5} \mathrm{m}^2$, n=0.06 m, R=0.05 m, $\rho = 1 \times 10^3$ kg/m^3. From the figure, it is evident that the measurement range of the sensor is approximately 20 L/s. When $m = 0.15$ kg, the variation in the output value M is about 0.45 , and the sensitivity is approximately 0.023 L/s. As the mass m of the torque body increases, the variation in the output value M decreases, with the sensitivity reducing to about 0.008 L/s. Thus, the sensitivity at $m = 0.15$ kg is roughly three times that at $m = 0.24$ kg. This indicates that changes in the torque body mass mmm significantly affect the sensor's sensitivity. Therefore, to enhance the sensor's sensitivity, a lower torque body mass should be selected in the design.

As shown in Figure 7, the $Q - M$ characteristic curves of the sensor were obtained for different radii r of the stress plate: 0.02 m, 0.022 m, 0.024 m, and 0.026 m. The remaining parameters were kept constant at $m = 0.15$ kg, $S_J = 5 \times 10^{-5}$ m^2, $n = 0.06$ m, $R = 0.05$ m, $\rho = 1 \times 10^3$ kg/m^3. The figure demonstrates that as the radius r of the stress plate increases, the change in the sensor output value M becomes more pronounced, particularly when the flow rate of the measured fluid ranges from12 L/s to 32 L/s. At radii of $r = 0.024$ m and 0.026 m, negative values appear in the figure. This occurs because, with a larger radius r of the stress plate and a higher flow rate, the rotation angle of the light baffle becomes large enough to fully block the receiving end face of the fiber bundle, causing the

receiving fiber to stop receiving signals. Consequently, the output value M reaches zero. The negative values shown in the figure are theoretical calculations and are included to illustrate the trend of the $Q - M$ characteristic curve; they do not reflect actual measurements. When $r = 0.02$ m, the sensor's sensitivity is approximately 0.023 L/s, whereas at $r = 0.026$ m, the sensitivity increases to about 0.083 L/s—around 3.6 times greater. Therefore, to effectively enhance the sensitivity of the sensor, designing a force plate with a larger radius is recommended.

As shown in Figure 8, the $Q - M$ characteristic curves of the sensor are plotted for different values of the fiber bundle end area S_J. According to Eq. (5), the sensor's output value M is determined by the ratio of the effective receiving area of the receiving fiber bundle to its total end area. Notably, the parameter a, which represents the width of the receiving fiber bundle's end face, does not affect the change in the output value M; it only influences the light intensity received by the receiving fiber bundle. Therefore, when analyzing the $Q - M$ characteristic curves, only the change in the receiving end height b of the fiber bundle needs to be considered. In this analysis, the values for b are 0.005 m, 0.006 m, 0.007 m, and 0.008 m, while a is fixed at 0.01 m. The remaining parameters are set to $m = 0.15$ kg, $r = 0.02$ m, $n = 0.06$ m, $R = 0.05$ m, and $\rho = 1 \times 10^3$ kg/m^3. The figure indicates that the sensitivity of the sensor decreases as the height b of the receiving fiber bundle's end face increases. Specifically, when $b = 0.005$ m, the sensor sensitivity is approximately 0.023 L/s, whereas at $b = 0.008$ m, the sensitivity decreases to about 0.012 L/s, which is roughly half the former value. To improve the sensor's sensitivity, a smaller receiving end height b should be selected once the fiber bundle end width a is determined. However, it is important to note that a smaller b value reduces the amount of light intensity coupled into the receiving fiber bundle, thereby diminishing the output light intensity signal, which could complicate subsequent signal processing. Therefore, while designing the sensor, b should not be too small.
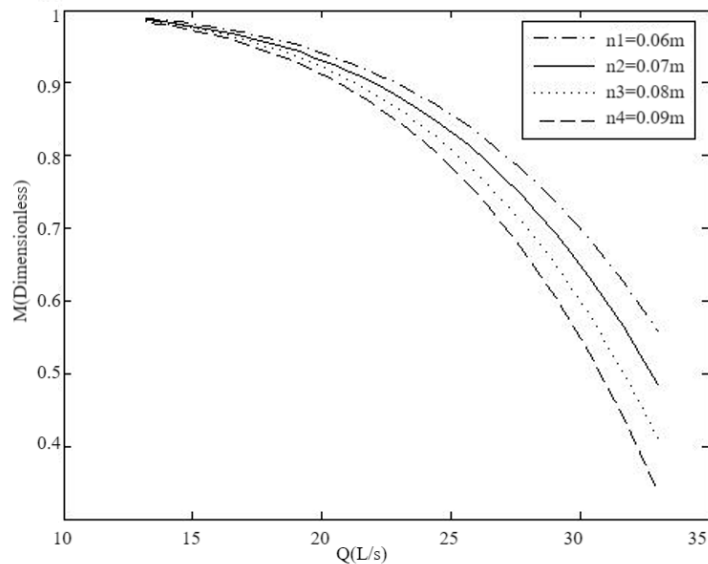

Figure 9. $Q - M$ Curve with change of n value

As shown in Figure 9, the $Q - M$ characteristic curves are presented for different values of the distance n from the axis center of the rotating shaft on the gravity swing rod to the lower edge of the light transmission hole, with n set to 0.06 m, 0.07 m, 0.08 m, and 0.09 m. The remaining parameters are kept constant at $m = 0.15$ kg, $r = 0.02$ m, $S_J = 5 \times 10^{-5}$ m^2, and $R = 0.05$ m. It can be observed from the figure that the sensitivity of the sensor increases with an increase in the value of n. When $n = 0.06$ m, the sensitivity is approximately 0.023 L/s, whereas for $n = 0.09$ m, the sensitivity rises to about 0.033 L/s, which is approximately 1.43 times higher. Therefore, to enhance the sensitivity of the sensor, a larger value of n can be considered in the design.

As shown in Figure 10, the $Q - M$ characteristic curves are plotted for different radii R of the flow channel of the measured fluid, with R set to 0.05 m, 0.06 m, 0.07 m, and 0.08 m. The remaining parameters are kept constant at $m = 0.15$ kg, $r = 0.02$ m, $S_J = 5 \times 10^{-5}$ m^2, and $n = 0.06$ m. Changes in the flow area affect the flow range detected by the sensor. This set of curves primarily illustrates the trend in the output value M of the fluid detected by the sensor at different flow rates when the structural parameters are fixed. The figure shows that a larger radius R of the flow pipe results in an increased sensor range but a decreased sensitivity. For $R = 0.05$ m, the range is approximately 20 L/s, with a sensitivity of about 0.023 L/s. In contrast, when $R = 0.08$ m, the range extends to around 45 L/s, and the sensitivity decreases to about 0.01 L/s. Therefore, the detection range of the sensor can be enhanced by increasing the radius of the flow channel.

As shown in Figure 11, the $Q - M$ characteristic curves are plotted for different densities ρ of the measured fluid,

respectively $\rho = 1 \times 10^3$ kg/m^3, $\rho = 1.1 \times 10^3$ kg/m^3, $\rho = 1.2 \times 10^3$ kg/m^3, and $\rho = 1.3 \times 10^3$ kg/m^3. The remaining parameters are set to $m = 0.15$ kg, $r = 0.02$ m, $S_J = 5 \times 10^{-5}$ m^2, $n = 0.06$ m, and $R = 0.05$ m. The figure indicates that the sensor's sensitivity increases with the density of the measured fluid. When detecting a fluid with a density of $\rho = 1 \times 10^3$ kg/m^3, the sensitivity is approximately 0.023 L/s, whereas for a fluid with a higher density $\rho = 1.3 \times 10^3$ kg/m^3, the sensitivity increases to about 0.038 L/s, which is approximately 1.65 times greater. Therefore, sensors with the same structural parameters exhibit higher sensitivity when detecting fluids with higher densities.
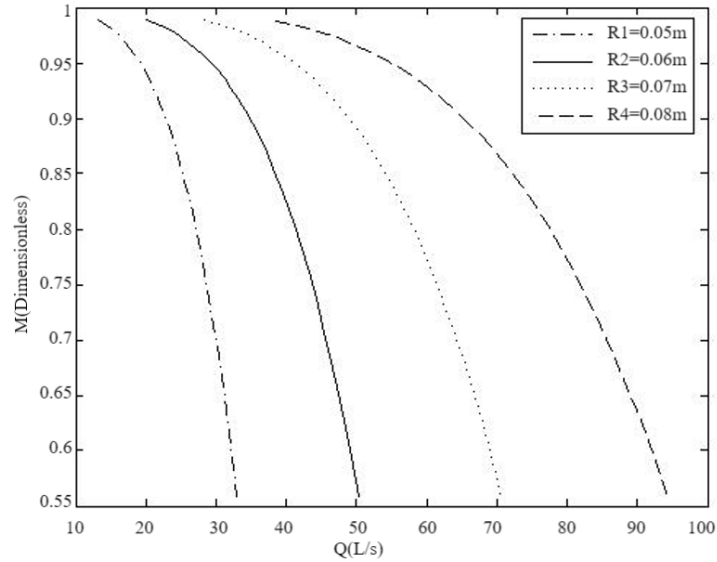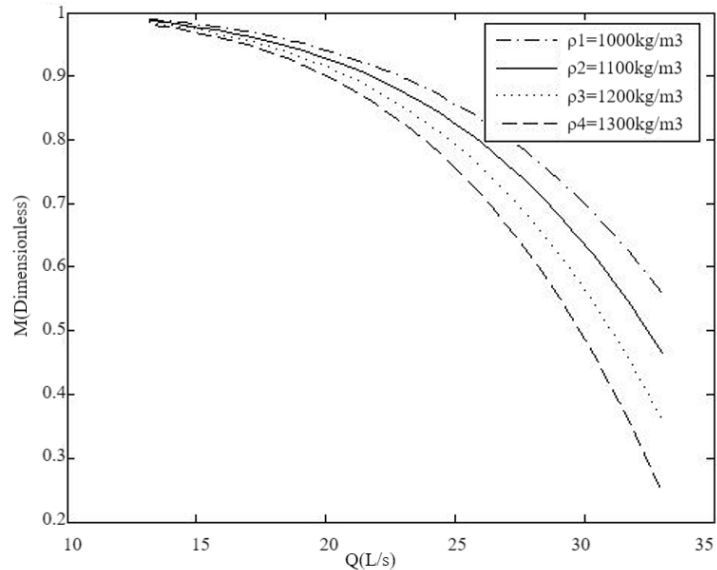

Figure 10. $Q - M$ Curve with change of R value

Figure 11. $Q - M$ Curve with change of ρ value

In summary, to effectively enhance the sensitivity of the sensor in the design of its structure, the following considerations should be made: a gravity swing rod with a smaller mass should be selected; a bearing plate with a larger radius is preferable; once the fiber bundle end width a is determined, a smaller fiber bundle receiving end height b should be chosen, although b should not be too small to avoid signal processing issues; and a larger value for n should be used. Additionally, to increase the sensor's range, the radius of the flow pipe can be enlarged.

5   Detection Experiment

Figure 12 shows the experimental prototype of the sensor. The setup primarily consists of an air source device, a gas storage tank, a flow control valve, a throttle valve, a sensor probe, a photoelectric converter, a signal processing module, and other components. During the experiment, the gas flow entering the sensor detection channel is varied by adjusting the opening of the flow control valve in the pneumatic circuit. The exhaust throttle valve is then adjusted to stabilize the gas flow through the detection channel. The gas flow is maintained at approximately 1.5 L/s, 1.8 L/s, 2.1 L/s, 2.4 L/s, 2.7 L/s, and 3.0 L/s for flow detection. The optical fiber probe utilizes a custom-made 5×5 rectangular array fiber bundle, consisting of 25 multimode fibers with a core diameter of 50 μm, to obtain the output detection signal at different flow rates. The resulting $\Delta Q - H$ curve is shown in Figure 13.
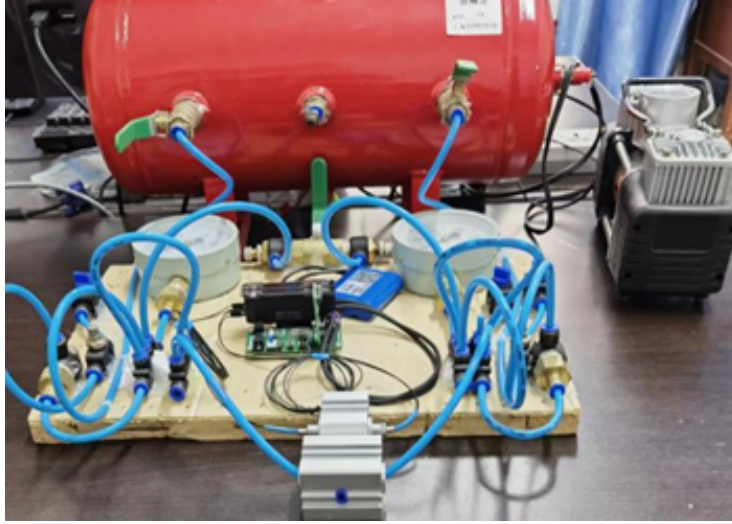
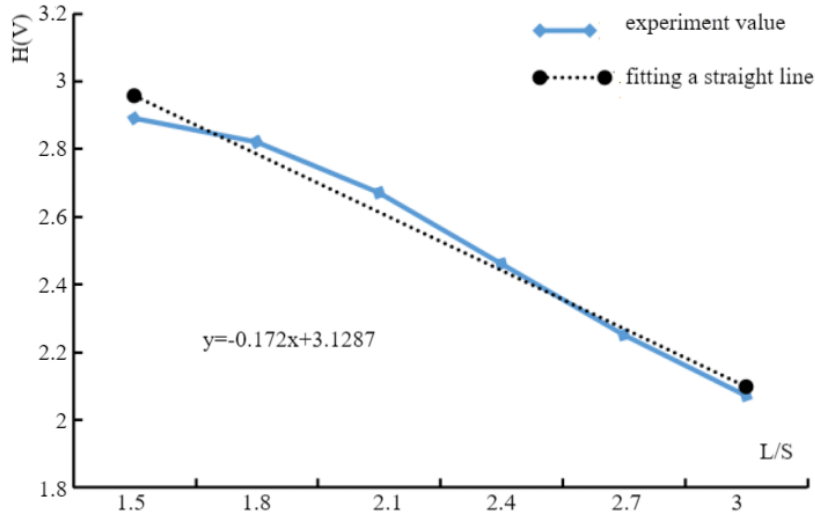

Figure 12. Sensor experimental prototype

Figure 13. $\Delta Q - H$ curve

As shown in Figure 13, the output signal H (in volts, V) decreases as the measured gas flow rate increases, and the $\Delta Q - H$ curve exhibits an approximately linear relationship. The fitted linear equation is provided below:

$$y = -0.172x + 3.1287 \tag{12}$$

From the figure, it is observed that the sensor's sensitivity is approximately 0.172 V/(L/s), with a linearity of about 4.7%. The experimental results closely align with the theoretical analysis curves presented earlier, thus validating the accuracy of the theoretical analysis process. This outcome also demonstrates that the new method of measuring fluid flow by combining the torque method with a rectangular array optical fiber bundle is effective.

6 Conclusions

A novel torque-based optical fiber flow sensor has been designed and experimentally evaluated in this study. (1) The sensor operates on the principle of optical fiber intensity modulation and is primarily composed of two parts: the mechanical package and the optical fiber bundle probe. The mechanical package includes an external shell, torque body, corrugated sealing bag, bearings, rollers, and other components, allowing the torque body to rotate freely within the shell when detecting fluid flow. The optical fiber bundle probe is divided into an incident fiber bundle and a receiving fiber bundle, both arranged in a rectangular array of multiple multimode fibers with small core diameters. The geometric shape and size of the two fiber bundles are identical, and the size of the light transmission hole on the torque body is consistent. (2) A sensing model for the sensor was established, and a simulation analysis was conducted based on this theoretical model. The analysis examined the effects of key parameters on the sensor's detection performance, including the mass m of the torque body, the radius r of the stress plate, the end area S_J of the fiber bundle, the distance n from the rotation axis of the torque body to the lower edge of the light transmission hole, the radius R of the fluid detection channel, and the density ρ of the fluid. $Q - M$ curves for each parameter were generated, and their influence on the sensor's performance was analysed. The results suggest that to effectively enhance the sensitivity of the sensor, a gravity swing rod with a smaller mass should be selected, along with a bearing plate with a larger radius. For a fixed fiber bundle end width a, a smaller fiber bundle receiving end height b is recommended, provided that b is not too small to avoid complications in signal processing. Additionally, a larger value of n should be chosen. To increase the sensor's range, the radius of the flow pipe can be enlarged. (3) The pneumatic system and the custom-made sensor probe were used to measure gas flow, and the sensor's $Q - M$ characteristic curve was obtained, followed by fitting a linear equation. The sensor demonstrated a sensitivity of approximately 0.172 V/(L/s) and a linearity of about 4.7%. The experimental results corroborated the theoretical analysis and demonstrated the effectiveness of the new method of measuring fluid flow by combining the torque method with a rectangular array optical fiber bundle.

Data Availability

The data used to support the research findings are available from the corresponding author upon request.

Conflicts of Interest

The authors declare no conflict of interest.

References

[1] F. Ejeian, S. Azadi, A. Razmjou, Y. Orooji, A. Kottapalli, M. E. Warkiani, and M. Asadnia, "Design and applications of MEMS flow sensors: A review," *Sens. Actuators, A*, vol. 295, pp. 483–502, 2019. https://doi.org/10.1016/j.sna.2019.06.020

[2] P. Liu, R. Zhu, and R. Y. Que, "A flexible flow sensor system and its characteristics for fluid mechanics measurements," *Sensors*, vol. 9, pp. 9533–9543, 2009. https://doi.org/10.3390/s91209533

[3] S. Ghosh, A. Sood, and N. Kumar, "Carbon nanotube flow sensors," *Science*, vol. 299, pp. 1042–1044, 2003. https://doi.org/10.1126/science.1079080

[4] N. Sabaté, J. Santander, L. Fonseca, I. Gràcia, and C. Cané, "Multi-range silicon micromachined flow sensor," *Sens. Actuators, A*, vol. 110, pp. 282–288, 2004. https://doi.org/10.1016/j.sna.2003.10.068

[5] E. A. Moro, M. D. Todd, and A. D. Puckett, "Performance optimization of bundled fiber optic displacement sensors," in *SPIE Smart Structures and Materials + Nondestructive Evaluation and Health Monitoring*, San Diego, United States, 2012, pp. 1112–1117. https://doi.org/10.1117/12.914707

[6] A. Leal-Junior, A. Theodosiou, A. Frizera-Neto, M. J. Pontes, E. Shafir, O. Palchik, N. Tal, S. Zilberman, G. Berkovic, P. Antunes, P. André, K. Kalli, and C. Marques, "Characterization of a new polymer optical fiber with enhanced sensing capabilities using a bragg grating," *Opt. Lett.*, vol. 43, pp. 4799–4802, 2018. https://doi.org/10.1364/ol.43.004799

[7] N. A. A. M. Arif, D. D. Burhanuddin, S. Shaari, and A. A. Ehsan, "Bend loss fiber optics design based on sinusoidal and ellipse configurations," *Opt. Appl.*, vol. LI, pp. 309–320, 2021. https://doi.org/10.37190/oa210301

[8] L. Schenato, A. Pasuto, A. Galtarossa, and L. Palmieri, "An optical fiber distributed pressure sensing cable with pa-sensitivity and enhanced spatial resolution," *IEEE Sens. J.*, vol. 20, pp. 5900–5908, 2020. https://doi.org/10.1109/JSEN.2020.2972057

[9] B. Lee, "Review of the present status of optical fiber sensors," *Opt. Fiber Technol.*, vol. 9, no. 2, pp. 57–79, 2003. https://doi.org/10.1016/S1068-5200(02)00527-8

[10] A. Taghipour, A. Rostami, M. Bahrami, H. Baghban, and M. Dolatyari, "Comparative study between LPFG- and FBG-based bending sensors," *Opt. Commun.*, vol. 312, pp. 99–105, 2014. https://doi.org/10.1016/j.optcom.2013.09.020

[11] L. Wei, Z. D. Zhou, J. Huang, and Y. He, "Study on non-contact mechanical vibration sensor with FBG," *China Mech. Eng.*, vol. 24, no. 14, pp. 1873–1876, 2013. https://doi.org/10.3969/j.issn.1004-132X.2013.14.006

[12] L. Schenato, Q. Rong, Z. Shao, X. Qiao, A. Pasuto, A. Galtarossa, and L. Palmieri, "Highly-sensitive FBG pressure sensor based on a 3D-printed transducer," *J. Lightwave Technol.*, vol. 37, no. 18, pp. 4784–4790, 2019. https://doi.org/10.1109/JLT.2019.2919917

[13] E. Vorathin, Z. M. Hafifizi, N. Ismail, and M. Loman, "Review of high sensitivity fibre-optic pressure sensors for low pressure sensing," *Opt. Laser Technol.*, vol. 121, p. 105841, 2020. https://doi.org/10.1016/j.optlastec.2019.105841

[14] L. Rindorf, P. E. Høiby, J. B. Jensen, L. H. Pedersen, O. Bang, and O. Geschke, "Towards biochips using microstructured optical fiber sensor," *Anal. Bioanal. Chem.*, vol. 385, pp. 1370–1375, 2006. https://doi.org/10.1007/s00216-006-0480-8

[15] H. E. Joe, H. Yun, S. H. Jo, M. B. Jun, and B. K. Min, "A review on optical fiber sensors for environmental monitoring," *Int. J. Precis. Eng. Manuf. Green Tech.*, vol. 5, pp. 173–191, 2018. https://doi.org/10.1007/s40684-018-0017-6

[16] P. Polygerinos, L. D. Seneviratne, and K. Althoefer, "Modeling of light intensity-modulated fiber-optic displacement sensors," *IEEE Trans. Instrum. Meas.*, vol. 60, no. 4, pp. 1408–1415, 2011. https://doi.org/10.1109/TIM.2010.2085270

[17] R. Nevshupa, M. Conte, and C. van Rijn, "Measurement uncertainty of a fiber-optic displacement sensor," *Meas. Sci. Technol.*, vol. 24, p. 035104, 2013. https://doi.org/10.1088/0957-0233/24/3/035104

[18] Z. N. Jia, K. Q. Yang, X. F. Zhao, Y. Bai, and H. Gao, "A new FBG thermal liquid flow sensor," *Acta Photonica Sinica*, vol. 50, no. 2, p. 0206002, 2021. https://doi.org/10.3788/gzxb20215002.0206002

[19] J. Li, J. Liu, C. Li, H. Zhang, and Y. Z. Li, "Wearable wrist movement monitoring using dual surface-treated plastic optical fibers," *Materials*, vol. 13, p. 3291, 2020. https://doi.org/10.3390/ma13153291

[20] R. Q. Lv, H. K. Zheng, Y. Zhao, and Y. F. Gu, "An optical fiber sensor for simultaneous measurement of flow rate and temperature in the pipeline," *Opt. Fiber Technol.*, vol. 45, pp. 313–318, 2018. https://doi.org/10.1016/j.yofte.2018.08.003

[21] A. Jderu, M. A. Soto, M. Enachescu, and D. Ziegler, "Liquid flow meter by fiber-optic sensing of heat propagation," *Sensors*, vol. 21, no. 2, p. 355, 2021. https://doi.org/10.3390/s21020355

[22] C. L. Lee, K. W. Liu, S. H. Luo, M. S. Wu, and C. T. Ma, "A hot-polymer fiber Fabry-Perot interferometer anemometer for sensing airflow," *Sensors*, vol. 17, no. 9, p. 2015, 2017. https://doi.org/10.3390/s17092015